

Cite this: *Nanoscale*, 2020, **12**, 9024

# Oxygen vacancy control as a strategy to achieve highly reliable hafnia ferroelectrics using oxide electrode

 Youngin Goh, <sup>†a</sup> Sung Hyun Cho,<sup>†b</sup> Sang-Hee Ko Park <sup>\*b</sup> and Sanghun Jeon <sup>\*a</sup>

Recently, hafnia ferroelectrics with two spontaneous polarization states have attracted marked attention for non-volatile, super-steep switching devices, and neuromorphic application due to their fast switching, scalability, and CMOS compatibility. However, field cycling-induced instabilities are a serious obstacle in the practical application of various low-power electronic devices that require a settled characteristic of polarization hysteresis. In this work, a large reduction in the field cycling-induced instabilities and significantly improved ferroelectric properties were observed in a  $\text{Hf}_{0.5}\text{Zr}_{0.5}\text{O}_2$  (HZO) thin film with a  $\text{RuO}_2$  oxide electrode. The oxide electrode can supply additional oxygen to the HZO film, consequently minimizing the oxygen vacancies at the interface which is the origin of low reliability. From the material and electrical analysis results, we verified that HZO with the  $\text{RuO}_2$  electrode has less non-ferroelectric dead layers and fewer oxygen vacancies at the interface, resulting in excellent switching properties and improved reliability. This result suggests a beneficial method to produce high-quality hafnia thin films free from interfacial defects and with stable field cycling electrical properties for actual applications.

Received 3rd February 2020,

Accepted 25th March 2020

DOI: 10.1039/d0nr00933d

rsc.li/nanoscale

## Introduction

With the increasing demand for low-power electronic devices, hafnia-based ferroelectric (FE) materials became a candidate for next-generation memory and logic devices such as non-volatile memory,<sup>1,2</sup> negative capacitance field effect transistors,<sup>3–5</sup> energy harvesters,<sup>6</sup> and neuromorphic applications.<sup>7,8</sup> Compared to the conventional perovskite FE thick film that has a high-quality single-crystalline phase, a hafnia-based FE thin film with a fluorite structure has mixed monoclinic (m), tetragonal (t), and orthorhombic (o) phases.<sup>9,10</sup> The ferroelectric behavior of the doped- $\text{HfO}_2$  films is believed to stem from the formation of the non-centrosymmetric o-phase under mechanical stress from the capped metal during annealing and cooling processes.<sup>11–13</sup> There are many merits for using hafnia-based FE instead of conventional FE in various electronic devices, including high scalability, fast switching speed, low relative permittivity, and process compat-

ibility with complementary metal–oxide–semiconductor.<sup>14,15</sup> However, property change with field cycling, which is called the wake-up effect, is still a hurdle in the commercialization of ferroelectric hafnia-based materials.<sup>16–18</sup>

In the binary computer memory, the stability of 0 and 1 states should be maintained for endurance cycles (write/erase cycles). In hafnia ferroelectrics, interestingly, the remnant polarization ( $P_r$ ) increases with cycling, which is the result of de-pinning of the pinned domains at the interface and a decrease in the local built-in field inside the film.<sup>16,19</sup> It has been reported that oxygen vacancy is inevitably produced in the interfacial region due to the reaction between metal and doped- $\text{HfO}_2$  film during the deposition and annealing processes. These regions are largely composed of the non-FE tetragonal phase  $\text{HfO}_{2-x}$  (sub-oxide) that is deemed non-switching in the pristine state, resulting in pinned FE domains and a pinched hysteresis curve.<sup>16</sup> When the bipolar endurance cycle is applied, the oxygen vacancy defects are redistributed and the pinned domains are removed. In addition, the interfacial non-FE t-phase is transformed into the FE o-phase, indicating an increased remnant polarization.<sup>19</sup>

In many previous papers, oxygen vacancies play a crucial role in stabilizing the FE o-phase in hafnia ferroelectrics.<sup>20</sup> They claimed that oxygen vacancies in hafnia induce the higher fraction of t-phase which can transform to o-phase leading to higher polarization. However, a lot of oxygen

<sup>a</sup>School of Electrical Engineering, Korea Advanced Institute of Science and Technology (KAIST), 291 Daehak-ro, Yuseong-gu, Daejeon 34141, Korea. E-mail: jeonsh@kaist.ac.kr

<sup>b</sup>Material Science and Engineering, Korea Advanced Institute of Science and Technology (KAIST), 291 Daehak-ro, Yuseong-gu, Daejeon 34141, Korea. E-mail: shkp@kaist.ac.kr

<sup>†</sup>These authors contributed equally to this work.

vacancy lead to earlier breakdown behavior and also influence on the wake-up effect. In this paper, the influence of metal oxide on the wake-up effect and ferroelectricity of  $\text{Hf}_{0.5}\text{Zr}_{0.5}\text{O}_2$  (HZO) FE thin film was systematically examined, using two electrode materials, TiN and  $\text{RuO}_2$ . The metal nitride TiN is widely used in the electrode of hafnia-based FE capacitors, but is easily oxidized into  $\text{TiO}_x\text{N}_y$  or  $\text{TiO}_2$  during the fabrication process, forming oxygen vacancy in the HZO film and dead layer at the interfacial region. In contrast, the metal oxide  $\text{RuO}_2$  can supply additional oxygen to the HZO film, lowering the vacancy defect of the HZO film and improving the stability of its polarization states with field cycling. Furthermore,  $\text{RuO}_2$  has excellent properties such as a high work function ( $\sim 5.1$  eV vs.  $\sim 4.2$  eV for TiN), low sheet resistivity, and high chemical stability.<sup>21,22</sup> Microscopic analysis with X-ray photoelectron spectroscopy (XPS) revealed that the HZO film with  $\text{RuO}_2$  electrode contained a smaller portion of non-ferroelectric sub-oxide ( $\text{HfO}_{2-x}$  and  $\text{ZrO}_{2-x}$ ) compared to that with TiN electrode. Electrical measurement using the pulse-switching techniques also verified that the  $\text{RuO}_2$  electrode could reduce the interfacial dead layer in HZO, which is one of the root causes of the wake-up effect.

## Experimental methods

### Device fabrication

We fabricated four different structures of the metal–ferroelectric–metal (MFM) capacitor to investigate the effect of  $\text{RuO}_2$  on the ferroelectricity and reliability of HZO film at both the top and bottom sides. The structures are [TiN/HZO/TiN], [TiN/HZO/ $\text{RuO}_2$ ], [ $\text{RuO}_2$ /HZO/TiN], and [ $\text{RuO}_2$ /HZO/ $\text{RuO}_2$ ]; abbreviated as TT, TR, RT, and RR, respectively.

First, 50 nm-thick TiN bottom electrodes were deposited on a  $\text{SiO}_2/\text{Si}$  substrate by physical vapor deposition (PVD) at 300 °C, and 10 nm-thick  $\text{RuO}_2$  bottom electrodes were deposited on the TiN/ $\text{SiO}_2/\text{Si}$  substrate by thermal atomic vapor deposition (ALD) with a  $\text{Ru}(\text{EtCp})_2$  precursor and  $\text{O}_2$  reactant at 225 °C. For the deposition of bottom  $\text{RuO}_2$  electrode on  $\text{SiO}_2/\text{Si}$ , it requires long incubation time because  $\text{SiO}_2$  has high surface energy, making it difficult to deposit 10 nm (around 10 days). Therefore,  $\text{RuO}_2$  was deposited on TiN with relatively low surface energy. Then, a 10 nm-thick HZO thin film was prepared on the TiN or  $\text{RuO}_2$  bottom electrode by thermal ALD with tetrakis(ethylmethylamino) hafnium (TEMA Hf) and tetrakis(ethylmethylamino) zirconium precursor  $\text{ZrO}_2$  and ozone ( $\text{O}_3$ ) reactant at 300 °C. After depositing the ferroelectric layer, a top electrode (25 nm for TiN or 10 nm for  $\text{RuO}_2$ ) was deposited using the same method. Finally, for electrical measurement, 10 nm Ti/30 nm Pt was deposited as a contact pad by using an E-beam evaporator through a  $70\ \mu\text{m} \times 70\ \mu\text{m}$  shadow mask. The TiN top electrode was chemically etched by  $\text{NH}_4\text{OH}:\text{H}_2\text{O}_2:\text{H}_2\text{O}$  solution (1 : 2 : 5), and the  $\text{RuO}_2$  top electrode was dry-etched with  $\text{O}_2$  plasma. Afterwards, all MFM capacitors were crystallized from the m-phase to the non-

centrosymmetric o-phase by rapid thermal annealing (RTA) at 600 °C for 10 s under an  $\text{N}_2$  atmosphere.

### Material analysis

The crystal structure and residual stress of the HZO thin film were analyzed from the patterns of grazing incidence X-ray diffraction (GIXRD, Rigaku diffractometer D/MAX-2500). In addition, to estimate the amount of oxygen vacancy, the ratios of sub-oxides  $\text{HfO}_{2-x}$  and  $\text{ZrO}_{2-x}$  in the HZO thin film at the top and bottom interfaces were quantitatively measured using XPS (K-alpha Thermo VG Scientific).

### Electrical analysis

To evaluate the ferroelectric switching properties, polarization–electric field ( $P$ – $E$ ) hysteresis curves were measured with a triangular bipolar pulse profile at  $3.5\ \text{MV cm}^{-1}$  using a ferroelectric tester (Radiant Technology, Precision LC II). The interfacial dead layer was determined using the pulse switching technique, by applying a trapezoidal pulse (rise and fall times: 10 ns, pulse width: 5  $\mu\text{s}$ ) from a semiconductor parameter analyzer (Keithley 4200 with 4225-PMU module). In addition, the endurance and retention properties of the HZO thin films were examined.

## Results and discussion

First, the influence of the top and bottom electrodes on the ferroelectric switching properties with field cycling was investigated by  $P$ – $E$  hysteresis measured from the initial sweep to  $10^4$  cycles. As shown in Fig. 1a, for all samples, both the  $+P_r$  and  $-P_r$  values increased during the cycling. However, those topped with  $\text{RuO}_2$  (RT and RR) hardly increased on the  $-P_r$  side. The exact increase rate of  $\pm P_r$  vs. number of cycles is plotted in Fig. 1b. From the plot, the increase rates of  $-P_r$  for RT and RR are only approximately 50% those for TT and TR, while those of  $+P_r$  are similar for all four devices. The values of  $P_r$  and the coercive field ( $E_c$ ) for all devices are summarized in Fig. 1c. The polarization values of TR and RT are approximately  $25\ \mu\text{C cm}^{-2}$ , much higher than those of TT ( $\sim 17\ \mu\text{C cm}^{-2}$ ) and RR ( $\sim 19\ \mu\text{C cm}^{-2}$ ). This was ascribed to the different thermal expansion coefficients of the bottom and top electrode materials (TiN:  $\sim 9.1 \times 10^{-6}\ \text{K}^{-1}$ ,  $\text{RuO}_2$ :  $\sim 6.4 \times 10^{-6}\ \text{K}^{-1}$ ), which induce a high in-plane tensile stress that is the main reason for forming the FE o-phase in the HZO film. The GIXRD patterns in Fig. 1d also verify that all devices are polycrystalline including the m, t, and o-phases, while the peak intensity for the o-phase ( $2\theta = 30.5^\circ$  and  $35.1^\circ$ ) is much higher for TR and RT as compared to TT and RR, corresponding to the electrical properties from the  $P$ – $E$  hysteresis curve.

To understand the different wake-up characteristics of the devices, we measured the XPS depth profile of Hf 4f and Zr 3d (Fig. 2). The remnant polarization increases with the cycles because of the de-pinning of the pinned domains at the interfacial oxygen vacancy defect.<sup>16</sup> It has been reported that oxygen vacancy is inevitably and primarily produced in the

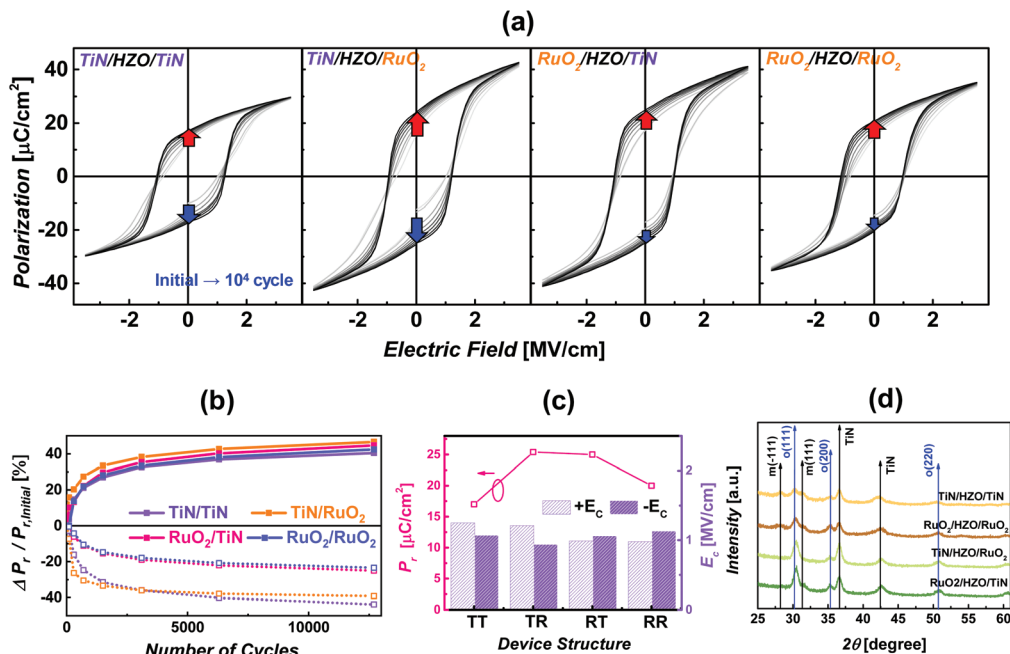


Fig. 1 (a) Polarization–electric field ( $P$ – $E$ ) characteristics of HZO thin films with different top and bottom electrodes (TT, TR, RT, RR). (b) Summary of remnant polarization ( $P_r$ ) value and  $\pm$ coercive electric-field ( $E_c$ ) value. (c) Increase rate of remnant polarization for 4 devices. (d) GIXRD patterns of 4 devices.

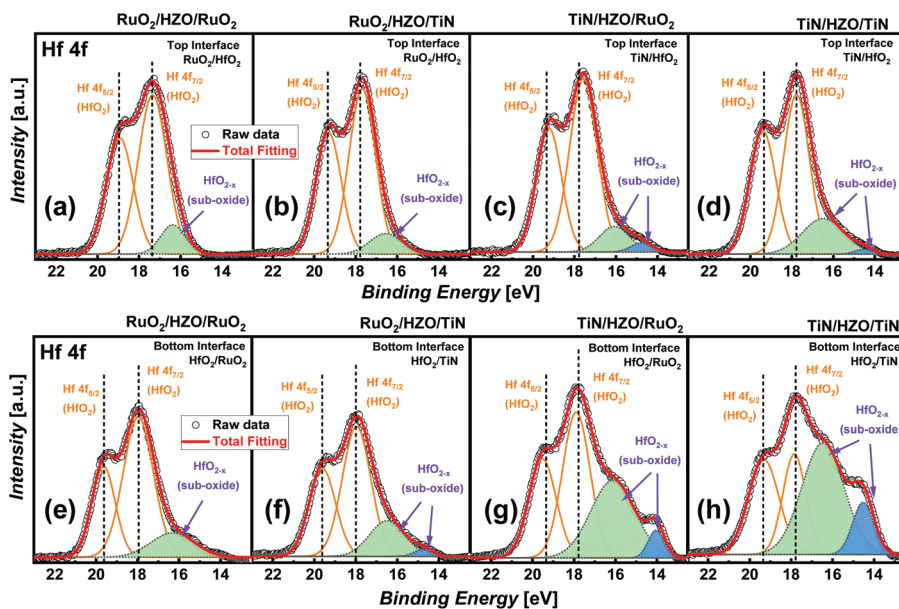


Fig. 2 XPS Hf 4f spectra in top electrode and HZO interface of (a) RuO<sub>2</sub>/HZO/RuO<sub>2</sub>, (b) RuO<sub>2</sub>/HZO/TiN, (c) TiN/HZO/RuO<sub>2</sub>, and (d) TiN/HZO/TiN. Hf 4f core level spectra in HZO and bottom electrode interface of (e) RuO<sub>2</sub>/HZO/RuO<sub>2</sub>, (f) RuO<sub>2</sub>/HZO/TiN, (g) TiN/HZO/RuO<sub>2</sub>, and (h) TiN/HZO/TiN.

interfacial region from the reaction between metal and HZO film during the deposition and annealing processes. Therefore, we can explain the wake-up effect of the four devices by analyzing the ratio of sub-oxide in the HZO thin film at both the top and bottom interface regions using XPS. From XPS depth profile, MFM devices was etched every 60 s by Ar ion, therefore we can define each layers and interfacial

region. Fig. 2a–d show the Hf 4f spectrum of RR, RT, TR, and TT, respectively, at the top interface; while Fig. 2e–f represent those at the bottom interface. The Hf 4f peaks for HfO<sub>2</sub> are located at 14.77 and 16.07 eV, and for sub-oxide they are located at 17.57 and 19.23 eV.<sup>23</sup> The sub-oxide is ascribed to the HfO<sub>2</sub> phase with defects such as oxygen vacancy and interstitial compounds. From the Hf 4f and Zr 3d spectra, the area

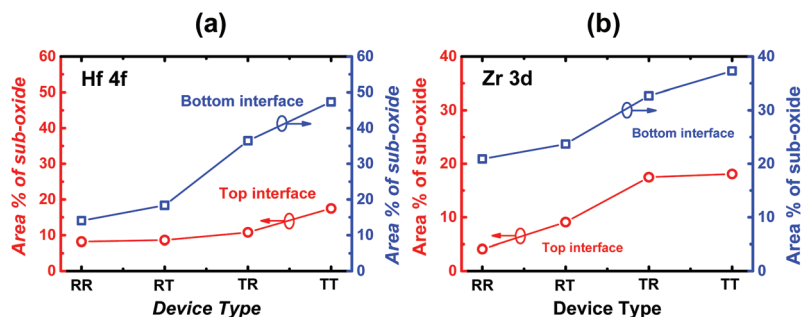


Fig. 3 The relative ratio of sub-oxide in (a)  $\text{HfO}_2$  and (b)  $\text{ZrO}_2$  for both top and bottom interface.

percentage of sub-oxide at the top and bottom interfaces is summarized in Fig. 3a and b, respectively. For all devices, the bottom interface contained much more sub-oxide than the top interface, as it goes through HZO deposition at 300 °C and post-metallization annealing at 600 °C. In addition, RR has the lowest level of sub-oxide while TT has the highest level according to both Hf 4f and Zr 3d spectra ( $\text{RR} < \text{RT} < \text{TR} < \text{TT}$ ), which is consistent with the lower increase rate of  $-P_r$  for RR and RT during cycling (Fig. 1b). Therefore, the  $\text{RuO}_2$  oxide electrode, especially when it is used as the top electrode, effectively suppresses the oxygen vacancy in HZO by providing oxygen to the HZO film. The same conclusion is supported by the Ru 3d core-level spectra. Fig. 4a shows Ru 3d spectra measured for three layers from the bulk to the interface with Ar ion etching. The  $\text{RuO}_2$  ( $\text{Ru}^{4+}$ ) component at 280.7 eV gradually decreases

toward the film interface, indicating that the interfacial  $\text{RuO}_2$  is reduced to Ru and provides oxygen to the HZO film.<sup>24</sup> In contrast, in the case of TiN,  $\text{TiO}_2$  components at 458.6 and 464.3 eV were observed in the Ti 2p spectrum, implying that the TiN electrode is easily oxidized into  $\text{TiO}_2$  and takes oxygen away from the HZO film (Fig. 4b). As a result, there is a significant amount of defect and vacancy in the HZO film with TiN electrode, leading to instability of polarization cycling with field cycling (the wake-up effect).

One interesting result is that between the TR and RT devices, TR shows more vacancy and a large wake-up effect. To confirm the quality of  $\text{RuO}_2$  at the top and bottom sides, O 1s XPS profiles were measured for  $\text{RuO}_2/\text{HZO}$  and  $\text{RuO}_2/\text{TiN}$  as shown in Fig. 4c. In the first case ( $\text{RuO}_2$  electrode deposited atop HZO FE film), most of the O 1s peak is related to oxygen bonded to Ru as  $\text{RuO}_2$ , meaning that there is no  $\text{RuO}_2$  reduction (top of Fig. 4c). In contrast, in  $\text{RuO}_2/\text{TiN}$  (bottom  $\text{RuO}_2$  electrode prepared on TiN substrate), the  $\text{RuO}_2$  reacts with TiN and is considerably reduced to Ru even before HZO deposition (bottom of Fig. 4c). From these results, we speculate that top  $\text{RuO}_2$  electrode can offer oxygen to the HZO film in a much more effective manner than as the bottom electrode. This is consistent with the fact that  $+P_r$  increased almost similarly for all devices, while the  $-P_r$  increase rate was reduced only in RT and RR. Table 1 summarizes the percentages of  $\text{RuO}_2$ , oxygen vacancy ( $\text{V}_\text{O}$ ), and weakly bound oxygen ( $\text{H}_2\text{O}$ ,  $\text{O}_2$ ) for each top and bottom  $\text{RuO}_2$  electrode.

To electrically measure the effect of  $\text{RuO}_2$  and TiN electrodes on the formation of non-FE interface layer, the short pulse switching technique was adopted.<sup>19</sup> Firstly, a negative write pulse was applied to align the polarization in one direction, and then the switching current ( $I_{\text{SW}}$ ) was obtained by applying a positive read pulse with different amplitudes from 2.4 to

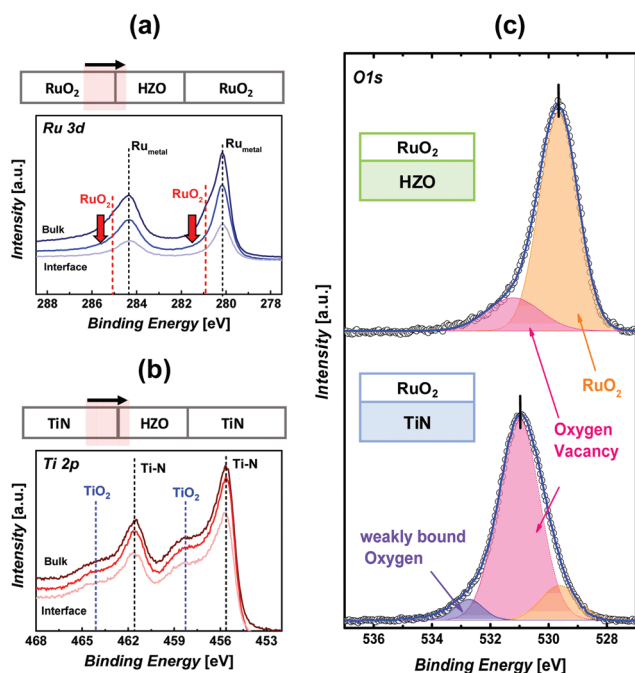


Fig. 4 XPS depth profile spectra for (a) Ru 3d of top interface in TiN/HZO/TiN device, and for (b) Ti 2p of top interface in  $\text{RuO}_2/\text{HZO}/\text{RuO}_2$  device. (c) XPS O 1s levels in bulk  $\text{RuO}_2$  layer deposited on HZO and TiN substrate.

Table 1 Comparison of the area percentage of  $\text{RuO}_2$  (529.6 eV) and oxygen vacancy (531.02 eV) and weakly bounded oxygen ( $\text{H}_2\text{O}$ ,  $\text{O}_2$ ) (532.7 eV) of  $\text{RuO}_2$  film deposited on the HZO and TiN

	$\text{RuO}_2$ (529.6)	$\text{V}_\text{O}$ (531.02)	$\text{H}_2\text{O}$ , $\text{O}_2$ (532.7)
$\text{RuO}_2$ on HZO	82.63%	17.36%	0
$\text{RuO}_2$ on TiN	12.33%	82.22%	5.45%

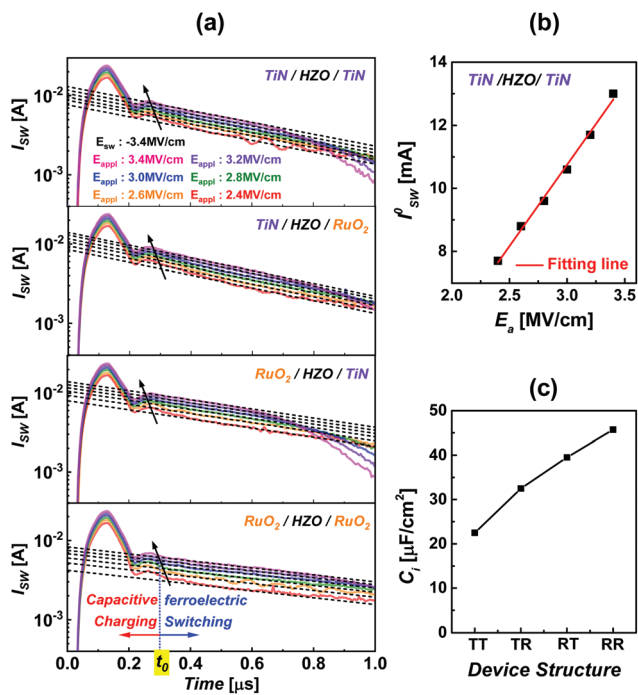


Fig. 5 (a) Transient domain switching current curves of 4 devices (TT, TR, RT, RR). (b) Representative data of switching starting current ( $I_{SW}^0$ ) as a function of the applied electric field ( $E_a$ ) for TiN/HZO/TiN devices. (c) Calculated interfacial capacitance ( $C_i$ ) values of 4 devices (TT, TR, RT, RR).

$3.4 \text{ MV cm}^{-1}$ . Fig. 5a shows the transient switching current of the four devices. According to the polarization reversal theory,  $I_{SW}$  can be defined by the following eqn (1),

$$I_{SW}(t) = I_{SW}^0 e^{(t-t_0)/R_L C_i} \quad (t_0 < t < t_{sw}) \quad (1)$$

where  $t_0$  and  $t_{sw}$  are the starting and finishing times of switching,  $I_{SW}^0$  is the switching current at  $t_0$ ,  $R_L$  is the total internal resistance, and  $C_i$  is the non-FE interfacial capacitance. This pulse switching technique supposes that the FE capacitor has an interfacial capacitance ( $C_i$ ) due to non-FE layer which is constant during pulse applying time leading to two different current behavior; (1) charging current flows of overall capacitor with time constant,  $R_L C_i$ , (2) unchanging switching current flow into the FE layer. At the beginning of the transient current, a rapid increase and decrease of  $I_{SW}$  were observed, which is related to the charging behavior of the MFM capacitor. After that, at  $t = t_0$ , represented by the arrow within the Fig. 5(a), the FE switching is started, and the switching current flows linearly through the capacitor, indicating that the HZO film acts as a resistor. Therefore, by fitting the linear region using eqn (1), we can extract the interfacial capacitance of non-ferroelectric layer except ferroelectric layer. Then,  $I_{SW}^0$  can be expressed by eqn (2)

$$I_{SW}^0(t) = (E_a - E_c) \cdot t_f / R_L \quad (2)$$

where  $E_a$ ,  $E_c$ , and  $t_f$  are the applied field, the coercive field, and the thickness of the FE layer, respectively. From this equation,

we can extract  $E_c$  and  $R_L$  from the plot of  $I_{SW}^0$  vs.  $E_a$  by obtaining the x-axis intercept and the slope, as shown in Fig. 5b. Finally, the interfacial capacitance  $C_i$  can also be extracted by substituting the  $R_L$  value in eqn (1). This switching kinetics assumes that the MFM capacitor has a non-FE interfacial capacitance ( $C_i$ ). From general physics, a high  $C_i$  value means a thinner interfacial non-FE layer. Fig. 5c shows the  $C_i$  values of the four devices. TT has the lowest  $C_i$  value and RR has the highest, indicating that TT has a relatively thick non-FE phase at the interface while RR has less of it and better quality in the FE thin film. This is consistent with the  $P$ - $E$  wake-up effect and the result of XPS analysis.

We also examined the switching speed of FE domains by measuring the change in polarization  $\Delta P(t)$  under applied square pulses with various widths.<sup>25</sup> The pulse sequence is shown in Fig. 6a. We first applied a negative pulse of sufficient time (20  $\mu\text{s}$ ) to polarize all domains, followed by the positive pulses  $P_{sw,1}$  (switching pulse) and  $P_{ns,1}$  (non-switching pulse). By subtracting the polarization under non-switching pulse from that of switching pulse, we obtained twice the saturated polarization ( $2P_s$ ). After that, we applied negative write pulse with various widths (5 ns to 20  $\mu\text{s}$ ), and  $P_{sw,2}$  and  $P_{ns,2}$  were used for extracting the time-dependent change in polarization,  $\Delta P(t)$ . Fig. 6b shows the relative ratio of time-dependent polarization change ( $\Delta P(t)/2P_s$ ) vs. the write pulse time ( $\log t$ ). For all four devices, the domains start switching at 10 ns, and whole domains can be switched within 400 ns. With the 100 ns pulse, the values of  $\Delta P(t)/2P_s$  are 88%, 81%, 72%, and 50% for RR, RT, TR, and TT, respectively. Thus, RR has the fastest switching speed due to the good quality of its interface, while the slowest switching speed of TT is attributed to defect or pinned domains at the interface.

Furthermore, the endurance and retention properties of TT and RR devices were measured to evaluate how the electrode affects the reliability of FE. Fig. 6c shows normalized remanent polarization ( $P_{r,normalized}$ ) values with number of cycles which exhibit the wake up and endurance characteristics of these two capacitors. In this graph, the initial  $P_r$  values of two devices were set to a certain value. By using this kind of plot, we can compare how much wake up occurs from the initial value for two different stacked devices. As a result, RR exhibited less wake up effect and better endurance until more than  $10^8$  cycles than TT ( $\sim 10^7$  cycles). This result was anticipated due to the charge injection through the defect and oxygen vacancy in TT that lead to early breakdown. In addition, the high work function of  $\text{RuO}_2$  causes low leakage current and high endurance characteristics. Fig. 7a shows the same state (SS), new same state (NSS) and opposite state (OS) retention measurements, which are well-known methods to measure the reliability of Ferroelectric Random Access Memory (FeRAM).<sup>26,27</sup> (The pulse profiles in Fig. 7a are for state 1, and we also measured those for state 2 by applying the opposite pulse.) The retention test was performed at 85  $^\circ\text{C}$  for 100 h with 5  $\mu\text{s}$  pulse width and  $\pm 3$  V pulse amplitude. The resulting read current for each SS, NSS, and OS state is normalized by the initial switched polarized extracted at room temperature,

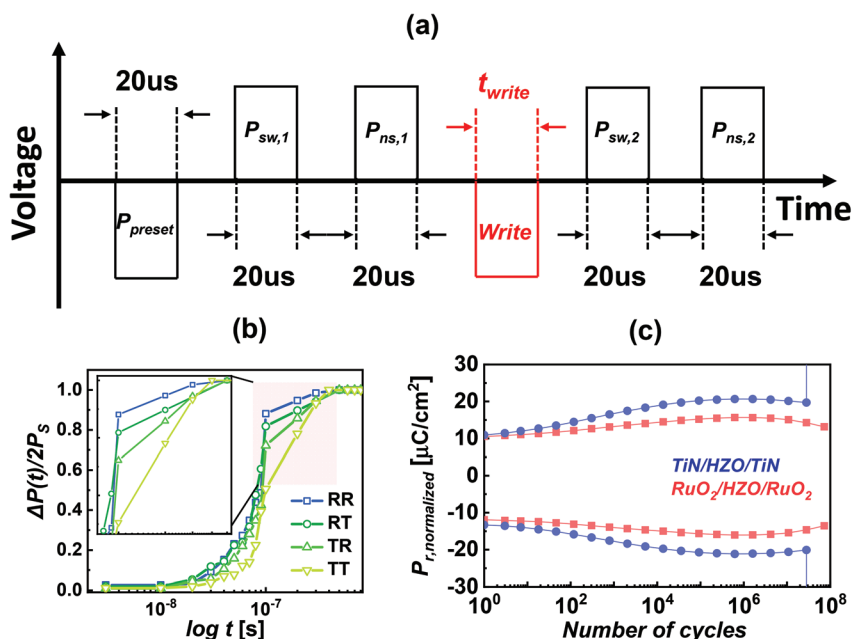


Fig. 6 (a) Sequences of pulse measurement. We can measure the saturation switching polarization ( $P_s$ ) and time-dependent polarization ( $\Delta P(t)$ ). (b) The relative ratio of time-dependent polarization ( $\Delta P(t)/2P_s$ ) according to write pulse time ( $t_{write}$ ). (c) Endurance characteristics of TT and RR devices with number of cycles.

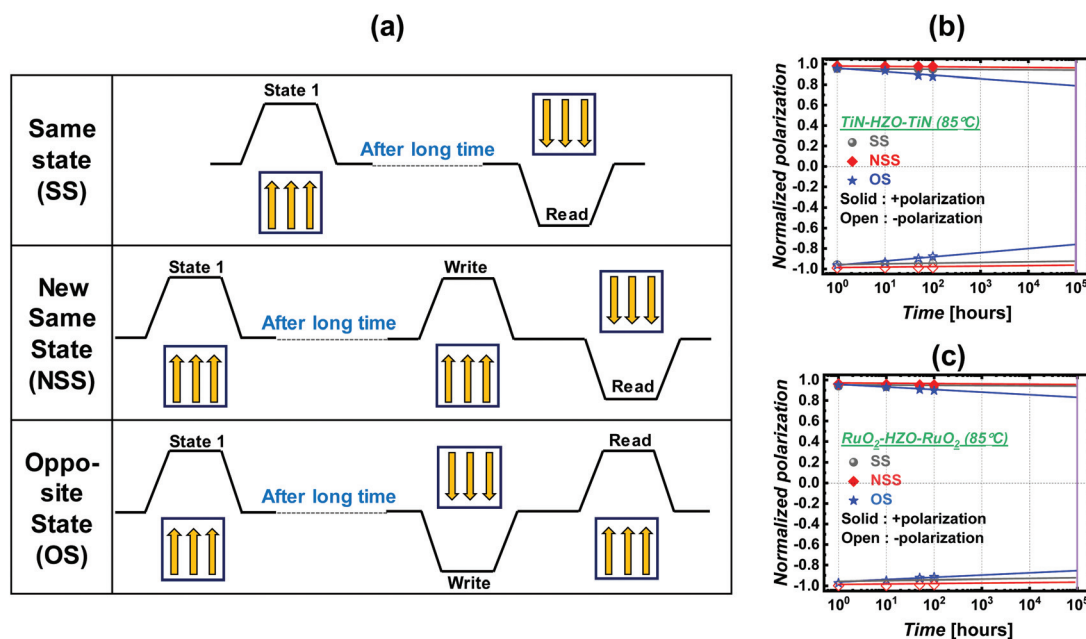


Fig. 7 (a) Pulse profiles of same state, new same state, and opposite state in case of non-switching and switching. Retention data by extrapolating the normalized polarization versus  $\log(\text{time})$  of (b) TiN/HZO/TiN and (c) RuO<sub>2</sub>/HZO/RuO<sub>2</sub> devices.

and the data were extrapolated to 10<sup>5</sup> h as shown in Fig. 7b and c. For both TT and RR devices, the SS and NSS retention characteristics are very clear and stable. However, RR shows better and stronger OS retention than the TT device, as TT should be more prone to thermal depolarization due to the built-in field created by vacancy in the interfacial regions.

Fig. 8a and b represent schematics of the possible species distribution inside the TT and RR devices from the combined results of material and electrical analysis. In the case of TT, the TiN transition metal electrode reacts with oxygen in the HZO layer, generating oxygen vacancies ( $V_O$ ) and defects in the HZO layer. Electron trapping at the vacancy creates a built-in

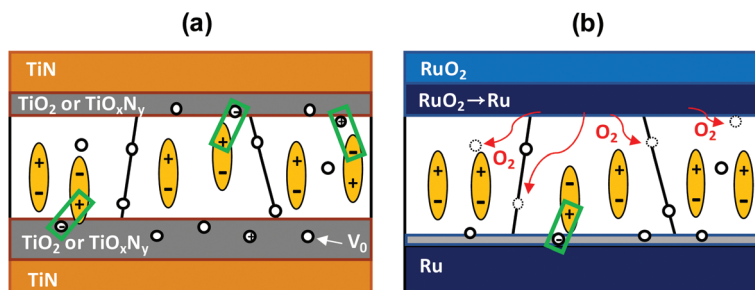


Fig. 8 The schematic diagram of the oxygen vacancy distribution and mechanism of wake up effect for (a) TiN/HZO/TiN and (b) RuO<sub>2</sub>/HZO/RuO<sub>2</sub>.

field inside the film and pinned domains that do not switch properly. As a result, the TT device shows a large wake-up effect and poor reliability. In contrast, the RuO<sub>2</sub> metal oxide electrode can supply oxygen to the HZO layer by its own reduction reaction, thereby suppressing oxygen vacancy formation. Thus, the RR device shows less interfacial layer, reduced wake-up effect, and excellent reliability.

## Conclusions

In this paper, we evaluate the effect of a metal oxide, RuO<sub>2</sub>, on the wake-up effect and reliability of HZO film by using various electrical and material analyses. The results of electrical measurement suggest that HZO with RuO<sub>2</sub> electrode exhibits less interfacial layer, reduced wake-up effect, and improved endurance and retention properties. This improvement can be explained by the suppression of oxygen vacancy, which is responsible for the wake-up effect and reliability degradation. The RuO<sub>2</sub> electrode can provide additional oxygen to the HZO layer to hinder the oxygen vacancy generation. This conclusion is also verified by the result of material measurement. According to the Hf 4f and Zr 3d core-level XPS profiles, RR shows the lowest ratio of sub-oxide (which is ascribed to the defects and oxygen vacancy) at the top and bottom interfaces. This effect of the RuO<sub>2</sub> electrode may provide an avenue to control the oxygen vacancy, in order to achieve highly reliable hafnia ferroelectrics that are essential for various memory applications.

## Conflicts of interest

There are no conflicts to declare.

## Acknowledgements

This work was supported by the Samsung Research Funding Center of Samsung Electronics under Project SRFCTA1703-01.

## Notes and references

- M. Dawber, K. M. Rabe and J. F. Scott, *Rev. Mod. Phys.*, 2005, **77**, 1083.
- Y. Goh and S. Jeon, *Nanotechnology*, 2018, **29**, 335201.
- S. Salahuddin and S. Datta, *Nano Lett.*, 2008, **8**, 405–410.
- K.-S. Li, P.-G. Chen, T.-Y. Lai, C.-H. Lin, C.-C. Cheng, C.-C. Chen, Y.-J. Wei, Y.-F. Hou, M.-H. Liao and M.-H. Lee, *IEEE Intl. Electron Devices Meet*, 2015, 22.6.1–22.6.4.
- M. Si, C.-J. Su, C. Jiang, N. J. Conrad, H. Zhou, K. D. Maize, G. Qiu, C.-T. Wu, A. Shakouri, M. A. Alam and P. D. Ye, *Nat. Nanotechnol.*, 2018, **13**, 24–29.
- M. H. Park, H. J. Kim, Y. J. Kim, T. Moon, K. D. Kim and C. S. Hwang, *Adv. Energy Mater.*, 2014, **4**, 1400610.
- L. Chen, T. Y. Wang, Y. W. Dai, M. Y. Cha, H. Zhu, Q. Q. Sun, S. J. Ding, P. Zhou, L. Chua and D. W. Zhang, *Nanoscale*, 2018, **10**, 15826–15833.
- Y. Goh and S. Jeon, *Appl. Phys. Lett.*, 2018, **113**, 052905.
- J. H. Choi, Y. Mao and J. P. Chang, *Mater. Sci. Eng., R*, 2011, **72**(6), 97–136.
- M. H. Park, Y. H. Lee, T. Mikolajick, U. Schroeder and C. S. Hwang, *Adv. Electron. Mater.*, 2019, **5**(3), 1800522.
- T. S. Böschke, J. Müller, D. Bräuhäus, U. Schröder and U. Böttger, *Appl. Phys. Lett.*, 2011, **99**(10), 102903.
- T. Shiraishi, K. Katayama, T. Yokouchi, T. Shimizu, T. Oikawa, O. Sakata, H. Uchida, Y. Imai, T. Kiguchi, T. J. Konno and H. Funakubo, *Appl. Phys. Lett.*, 2016, **108**(26), 262904.
- R. Cao, Y. Wang, S. Zhao, Y. Yang, X. Zhao, W. Wang, X. Zhang, H. Lv, Q. Liu and M. Liu, *IEEE Electron Device Lett.*, 2018, **39**(8), 1207–1210.
- S. Salahuddin, K. Ni and S. Datta, *Nat. Electron.*, 2018, **1**(8), 442.
- J. Müller, T. S. Böschke, D. Bräuhäus, U. Schröder, U. Böttger, J. Sundqvist, V. Sundqvist, P. Kücher and L. Frey, *Appl. Phys. Lett.*, 2011, **99**(11), 112901.
- M. Pešić, F. P. G. Fengler, L. Larcher, A. Padovani, T. Schenk, E. D. Grimley, X. Sang, J. M. LeBeau, S. Slesazeck, U. Schroeder and T. Mikolajick, *Adv. Funct. Mater.*, 2016, **26**(25), 4601–4612.
- Y. Goh and S. Jeon, *J. Vac. Sci. Technol., B: Nanotechnol. Microelectron.: Mater., Process., Meas., Phenom.*, 2018, **36**(5), 052204.
- M. H. Park, Y. H. Lee, T. Mikolajick, U. Schroeder and C. S. Hwang, *MRS Commun.*, 2018, **8**(3), 795–808.

- 19 H. J. Kim, M. H. Park, Y. J. Kim, Y. H. Lee, T. Moon, K. D. Kim, S. D. Hyun and C. S. Hwang, *Nanoscale*, 2016, **8**(3), 1383–1389.
- 20 M. Hoffmann, U. Schroeder, T. Schenk, T. Shimizu, H. Funakubo, O. Sakata, D. Pohl, M. Drescher, C. Adelman, R. Materlik, A. Kersch and T. Mikolajick, *J. Appl. Phys.*, 2015, **118**(7), 072006.
- 21 J. H. Kim, D. S. Kil, S. J. Yeom, J. S. Roh, N. J. Kwak and J. W. Kim, *Appl. Phys. Lett.*, 2007, **91**(5), 052908.
- 22 J. Si and S. B. Desu, *J. Mater. Res.*, 1993, **8**(10), 2644–2648.
- 23 I. K. Oh, B. E. Park, S. Seo, B. C. Yeo, J. Tanskanen, W. H. Kim and H. Kim, *J. Mater. Chem. C*, 2018, **6**(27), 7367–7376.
- 24 J. Balcerzak, W. Redzyna and J. Tyczkowski, *Appl. Surf. Sci.*, 2017, **426**, 852–855.
- 25 H. K. Yoo, J. S. Kim, Z. Zhu, Y. S. Choi, A. Yoon, M. R. MacDonald, X. Lei, T. Y. Lee, D. Lee, S. C. Chae, J. Park, D. Hemker, J. G. Langan, Y. Nishi and J. Park, In 2017 IEEE International Electron Devices Meeting (IEDM), 2017, (pp. 19–6).
- 26 S. Mueller, J. Muller, U. Schroeder and T. Mikolajick, *IEEE Trans. Device Mater. Reliab.*, 2012, **13**(1), 93–97.
- 27 J. Rodriguez, K. Remack, J. Gertas, L. Wang, C. Zhou, K. Boku, K. R. Rodriguez-Latorre, S. Udayakumar, S. Summerfelt and T. Moise, In 2010 IEEE International Reliability Physics Symposium, 2010, pp. 750–758.